

pubs.acs.org/acscatalysis Research Article

Variation in the In₂O₃ Crystal Phase Alters Catalytic Performance toward the Reverse Water Gas Shift Reaction

Jianyang Wang, Chun-Yen Liu, Thomas P. Senftle, Jie Zhu, Guanghui Zhang,* Xinwen Guo,* and Chunshan Song*



Cite This: ACS Catal. 2020, 10, 3264-3273



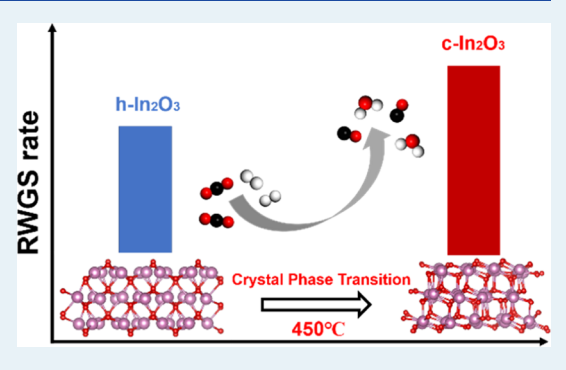
ACCESS

Metrics & More

Article Recommendations

3 Supporting Information

ABSTRACT: Understanding the structure—catalytic activity relationship is crucial for developing new catalysts with desired performance. In this contribution, we report the performance of In_2O_3 with different crystal phases in the reverse water gas shift (RWGS) reaction, where we observe changing activity induced by a phase transition under reaction conditions. Cubic In_2O_3 (c- In_2O_3) exhibits a higher RWGS rate than the hexagonal phase (h- In_2O_3) at temperatures below 350 °C because of its (1) enhanced dissociative adsorption of H_2 , (2) facile formation of the oxygen vacancies, and (3) enhanced ability to adsorb and activate CO_2 on the oxygen vacancies, as suggested both experimentally and computationally. Density functional theory results indicate that the surface oxygen arrangement on the cubic polymorph is key to rapid H_2 adsorption, which facilitates oxygen vacancy



formation and subsequent CO_2 adsorption to yield high RWGS reactivity. At 450 °C and above, the activity of h- In_2O_3 increases gradually with time on stream, which is caused by a phase transition from h- In_2O_3 to c- In_2O_3 . In situ X-ray diffraction experiments show that h- In_2O_3 is first reduced by H_2 and subsequently oxidized by CO_2 to c- In_2O_3 . These findings highlight the importance of the crystal phase in the catalytic RWGS reaction and provide a new dimension for understanding/designing RWGS catalysts.

KEYWORDS: In_2O_3 catalysts, crystal phase transition, reverse water gas shift reaction, oxygen vacancy, DFT simulations, in situ XRD

INTRODUCTION

In recent years, with growing energy demand and the burning of fossil fuel, a considerable amount of CO2 is emitted into the atmosphere, leading to increasing global temperature and ocean acidification, posing threats to the world's ecosystems. Therefore, developing techniques for catalytic CO₂ reduction to make higher-value products, such as fuels or key molecular building blocks for the chemical industry, is a promising way to ameliorate this threat. $^{1-5}$ CO₂ hydrogenation to CO, commonly known as the reverse water gas shift (RWGS) reaction, can be coupled with other processes, such as Fischer-Tropsch synthesis, and has thus been extensively studied as a CO₂ mitigation strategy.^{6–8} Among all known RWGS catalysts,^{9–20} In-based catalysts have excellent performance because of the large number of oxygen vacancies on the surface of these materials. Under methanol synthesis conditions, where shutting down RWGS is desirable, RWGS is inhibited on In₂O₃, and CO₂ does not adsorb and activate in oxygen vacancies in the cubic (110) surface. 21,22 However, under atmospheric pressure, CO is the main reaction product over In-based catalysts instead of methanol. Liu et al. developed a deep understanding of In-based catalysts combining theoretical calculations and experimental investigations. They elucidated the critical role of the oxygen vacancy and found that the catalytic activity of In₂O₃ can be enhanced by mixing In_2O_3 with CeO_2 to promote the formation of oxygen vacancies. ^{23,24} In many cases, the activity is heavily affected by the support, the particle size, and the crystal structure of the catalysts. ^{25,26}

It has been previously shown that catalysts/supports with different crystal phases show remarkably different performances, including the reaction rate, selectivity, and stability. The supported on TiO2, where the activity and product selectivity were strongly dependent on the TiO2 crystal phases. Song et al. also observed a similar phenomenon on Co/TiO2 catalysts with different TiO2 crystal phases exhibiting different performances for CO2 methanation. The Co/rutile—TiO2 catalyst selectively catalyzes CO2 hydrogenation to CH4, while CO is the main product on the Co/anatase—TiO2 catalyst. Based on a density functional theory (DFT)-based kinetic study, Li et al. found that CO activation on hexagonal close-packed (hcp) Co has much higher intrinsic activity than that of the face centered-cubic (fcc) phase in Fischer—Tropsch synthesis

Received: October 1, 2019
Revised: December 23, 2019
Published: December 24, 2019



because of the absence of favorable active sites for fcc Co.³³ Nie et al. experimentally found that hcp-Co indeed exhibits higher activity toward hydrocarbon formation than fcc-Co.³⁴

Crystalline $\rm In_2O_3$ exists in two predominant polymorphs, the cubic (bixbyite type) and hexagonal (corundum type), and most of the studies have been focused, both experimentally and theoretically, on the cubic form. ^{23,24,35-50} Hexagonal $\rm In_2O_3$ (h- $\rm In_2O_3$) has been studied far less than cubic $\rm In_2O_3$ (c- $\rm In_2O_3$). In this work, we compare the catalytic performance of c- $\rm In_2O_3$ and h- $\rm In_2O_3$ in the RWGS reaction. c- $\rm In_2O_3$ shows a higher RWGS rate than h- $\rm In_2O_3$ because of the facile formation of oxygen vacancies and stronger adsorption of $\rm CO_2$. We also show that under certain reaction conditions, h- $\rm In_2O_3$ transforms to c- $\rm In_2O_3$, leading to increasing catalytic RWGS performance.

■ EXPERIMENTAL SECTION

Synthesis of In₂O₃. c-In₂O₃ was prepared through the controlled calcination of $In(OH)_3$. Typically, 5.2 g of $In(NO_3)_3$ ·SH₂O was dissolved in 120 mL of deionized water, followed by the addition of NH₄OH (80 mL, 15 wt % in H₂O). After centrifugation and decantation, the precipitate was collected and washed with deionized water. c-In₂O₃ was obtained after drying the precipitate at 80 °C for 12 h and calcination at 490 °C for 2 h with a ramping rate of 2 °C/min in air. Prior to the RWGS reaction, c-In₂O₃ was treated at 430 °C for 2 h in mixture gas $(CO_2/H_2/N_2 = 28:56:16)$ at a flow rate of 60 mL/min.

h-In $_2$ O $_3$ was prepared by a modified solvothermal reaction. Oleic acid (40 mL), 20 mL of n-amyl alcohol, and 80 mL of n-hexane were first mixed. Eight milliliters of 0.5 mol/L In(NO $_3$) $_3$ and 8 mL 8 mol/L NaOH solutions were simultaneously added into this solution under vigorous stirring at 70 °C for 1 h. The obtained emulsion was added into an autoclave and heated at 200 °C for 40 h and then allowed to cool to room temperature. The precipitate was washed several times with absolute ethanol and deionized water, and then the sample was dried at 80 °C for 12 h and calcined at 490 °C for 2 h with a ramping rate of 2 °C/min in air. Prior to the RWGS reaction, h-In $_2$ O $_3$ was treated at 350 °C for 2 h in mixture gas (CO $_2$ /H $_2$ /N $_2$ = 28:56:16) at a flow rate of 60 mL/min.

Characterization. The X-ray diffraction (XRD) patterns of the fresh and spent catalysts were obtained using a Rigaku SmartLab 9kw diffractometer with Cu $K\alpha$ radiation (λ = 1.5406 Å) with a 0.02° step size over the range between 5 and 80°. In situ XRD measurements were performed in the XRK 900 reactor chamber made by Anton Paar Corporation. The catalyst powder was packed into the ceramic sample stage (internal diameter 15 mm). There are beryllium windows on the hermetic reactor chamber allowing the X-ray through. The temperature was controlled using a TCU 750 Temperature Control Unit. The XRD data were analyzed using the integrated PDXL2 software. The crystallite phases were identified by comparing the diffraction patterns with the data from the Joint Committee on Powder Diffraction Standards (JCPDS) database.

The textural properties of the samples were determined by N_2 adsorption on a Quantachrome AUTO-SORB-1-MP sorption analyzer at liquid nitrogen temperature (-196 °C). The specific surface area was determined by the Brunauer–Emmett–Teller (BET) method. In addition, the pore size distribution was obtained using the adsorption isotherm through the Barrett–Joyner–Halenda method. Prior to the

measurements, the catalysts were treated under vacuum at 300 $^{\circ}\text{C}$ for 2 h.

Scanning electron microscopy (SEM) images were obtained on a Hitachi S-5500 instrument with an acceleration voltage of 3 kV. High-resolution transmission electron microscopy (HRTEM) imaging was conducted to obtain clear lattice fringes of the catalysts, which were measured on a Tecnai F30 HRTEM instrument (FEI Corp.) operated at 300 kV. The samples for TEM analysis were prepared by dropping ethanol suspension of samples on the carbon film-coated copper grids.

H₂ temperature-programmed reduction (H₂-TPR) was conducted on a Chem BET Pulsar TPR/temperatureprogrammed desorption (TPD) equipment (Quantachrome, USA). About 100 mg of the sample was placed in a quartz tube in the furnace. To remove the moisture and other contaminants, the sample was flushed with He at 300 °C for 1 h and then cooled to room temperature. The sample was reduced with 5 vol % H₂/Ar at a flow rate of 30 mL/min and heated to 800 °C with a ramp rate of 10 °C/min. For removal of the water formed during the reduction, a cooling trap was placed between the sample and the thermal conductivity detector (TCD). TPD of CO₂ (CO₂-TPD) was performed using the same instrument as that used to measure H₂-TPR. The sample (200 mg) was reduced in 5 vol % H₂/Ar (30 mL/ min) at 300 °C for 1 h and then cooled to 50 °C, followed by CO₂ adsorption at 50 °C for 2 h. The sample was then flushed with N₂ with a flow rate of 30 mL/min and heated to 700 °C at a ramp rate of 5 °C/min. Desorbed species were monitored by TCD (TPD) and mass spectrometry (TPD-MS).

X-ray photoelectron spectroscopy (XPS) analysis was performed over a spectrometer (model Max 200, Leybold, Germany) using Al $K\alpha$ radiation as an excitation source.

Catalytic Testing. The CO₂ hydrogenation performance over c-In2O3 and h-In2O3 was evaluated in a continuous-flow fixed-bed reactor under 0.1 MPa (gauge pressure). The flow rate of the feed gas was controlled using a mass flow controller (Brooks 5850E). The reactor was heated by a Micrometrics Eurotherm 2416 furnace, while the catalyst bed temperature was monitored using a K-type thermocouple located at the center of the catalyst bed. Prior to the catalytic test, the catalyst (0.2 g) was packed into a quartz reactor (inner diameter 6 mm) and purged with N₂ at a flow rate of 60 mL/min at target temperature for 30 min. Then, the feed gas was switched to the CO_2 , H_2 , and N_2 mixture gas $(CO_2/H_2/N_2 = 28:56:16)$ at a flow rate of 60 mL/min. The gas products were analyzed online using an Agilent 7890B gas chromatograph with a TDX-01 column connected to a TCD. The catalytic performance was evaluated by the conversion of CO2 on the basis of the different concentrations between the outlet, which is defined as

$$x_{\rm CO_2} = \frac{n_{\rm CO_2}^{\rm in} - n_{\rm CO_2}^{\rm out}}{n_{\rm CO_2}^{\rm in}} \times 100\%$$
 (1)

The selectivity of CO and CH₄ is defined as follows

$$S_{\rm CO} = \frac{n_{\rm CO}^{\rm out}}{n_{\rm CO}^{\rm out} + n_{\rm CH_4}^{\rm out}} \times 100\%$$
 (2)

$$S_{\text{CH}_4} = \frac{n_{\text{CH}_4}^{\text{out}}}{n_{\text{CO}}^{\text{out}} + n_{\text{CH}_4}^{\text{out}}} \times 100\%$$
 (3)

where $n_{\rm CO}^{\rm out}$, $n_{\rm CH_4}^{\rm out}$, and $n_{\rm CO_2}^{\rm out}$ represent moles concentration of CO, CH₄, and CO₂ at the outlet of the reactor and $n_{\rm CO_2}^{\rm in}$ is the moles concentration of CO₂ in the feed.

Density Functional Theory. DFT was implemented with the Vienna ab initio simulation package (VASP 5.4.4). The projector augmented-wave method was applied to treat core electrons with default potentials in VASP, 3,54 while the Perdew–Burke–Ernzerhof (PBE) exchange–correlation functional was employed with spin polarization. The explicit valence electrons for each atom type were as follows: C—2s²2p², H—1s¹, In—5s²4d¹⁰5p¹, and O—2s²2p⁴. Monkhorst–Pack (MP) *k*-point mesh samplings were 2 × 2 × 1 for the c-In₂O₃(111) surface model and 3 × 3 × 1 for the h-In₂O₃(110) surface model. Each facet was chosen because it is the most thermodynamically stable facet of each phase, which is also reflected in the XRD analysis in Figure 1a. Plane wave basis

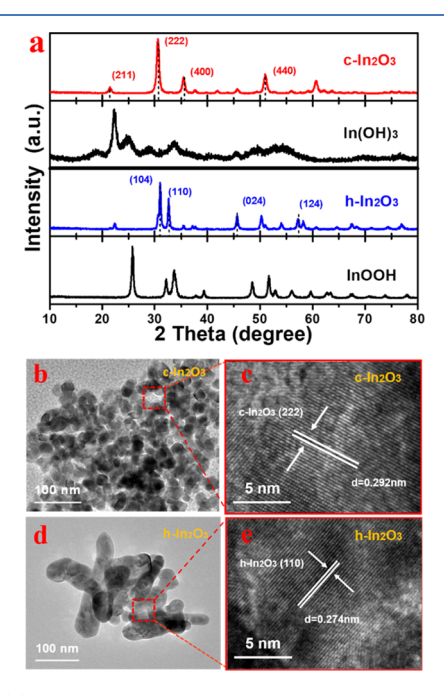


Figure 1. (a) XRD patterns of c-In₂O₃ and h-In₂O₃. (b,c) HRTEM images of c-In₂O₃ and (d,e) HRTEM images of h-In₂O₃.

sets were truncated at a kinetic energy cutoff of 700 eV, where Gaussian smearing was applied with a 0.05 eV width. A self-

consistent dipole correction perpendicular to the In₂O₃ surfaces was applied, as implemented in VASP. Geometries were optimized until forces converged to 0.05 eV/Å. The Grimme-D3 dispersion correction was included to treat van der Waals interactions.⁵⁸ Surface models included three layers of c-In₂O₃(111) and h-In₂O₃(110), where all layers were relaxed to avoid generating dipoles that can arise when freezing oxide layers on the reverse side of the slab.⁵⁹ The distance between the substrates in the periodic cell is at least 15 Å in the z direction. The energies of O2, H2, CO2, CO, and H2O were calculated in a 15 \times 16 \times 17 Å³ simulation cell with 1 \times 1 × 1 MP sampling. Because DFT with generalized gradient approximation (GGA) functionals is known to describe localized electrons incorrectly, we also tested the sensitivity of our results with respect to Dudarev's DFT + U formalism. For these tests, we employed a U value of 7 eV on the d electrons of In.⁶¹ We found that the U correction did not alter trends between the various In2O3 surfaces but did systematically shift adsorption energies. As such, both DFT and DFT + U adsorption energies are discussed in the Results and Discussion section.

Translational, rotational, and vibrational entropy corrections were computed using standard formulae derived from statistical mechanics, while only vibrational entropy was included for adsorbed species with no translational or rotational degrees of freedom. Most structures were confirmed to be true energy minima with no imaginary vibrational modes present after a frequency analysis with a finite difference of 0.02 Å. Only one structure (hydrogen adsorbed on the h-In₂O₃ (110) surface) had a recalcitrant imaginary frequency of 196.47 cm⁻¹ that could not be removed despite repeated optimization attempts with tighter convergence criteria (from 0.05 to 0.01 eV/Å), which we attribute to numerical noise. Details for accessing an online repository containing all coordinates for optimized structures and total DFT energies are provided in the Supporting Information.

Oxygen vacancy formation energy ($\Delta E_{\rm Ovac}$) and hydrogen adsorption energy ($\Delta E_{\rm Hads}$) at all surface sites were computed by eqs 4 and 5, respectively, where $E_{\rm In_2O_3}$ is the total DFT energy of the clean surface, $E_{\rm In_2O_3\text{-vac}}$ is the total DFT energy of the surface with one oxygen vacancy, $E_{\rm O_2}$ is the total DFT energy of the oxygen molecule, $E_{\rm H\text{-}In_2O_3}$ is the total DFT energy of the surface with one adsorbed hydrogen atom, and $E_{\rm H_2}$ is the total DFT energy of the hydrogen molecule.

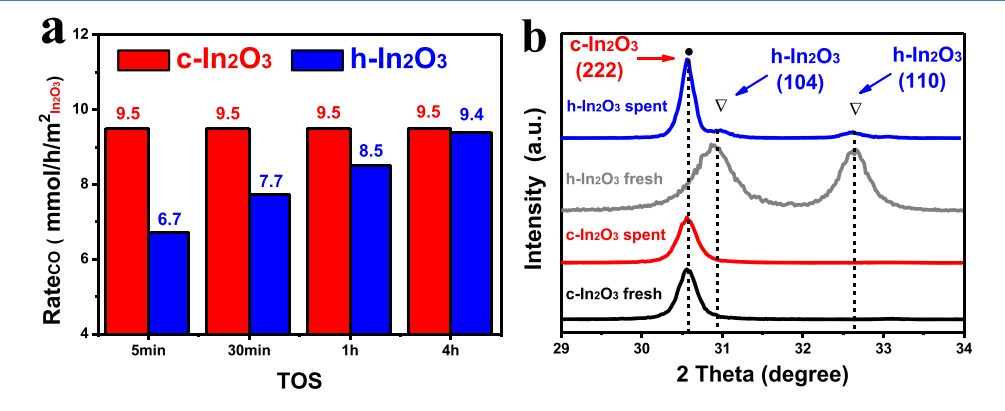


Figure 2. (a) Rate of CO formation over $c-In_2O_3$ and $h-In_2O_3$ normalized to the specific surface area and (b) XRD patterns of $c-In_2O_3$ and $h-In_2O_3$ (fresh and spent). Reaction conditions: 450 °C, TOS = 4 h, GHSV = 18 000 mL/g/h, $H_2/CO_2 = 2$, P = 0.1 MPa, CO selectivity > 99%.

$$\Delta E_{\text{Ovac}} = E_{\text{In}_2\text{O}_3\text{-vac}} + \frac{1}{2}E_{\text{O}_2} - E_{\text{In}_2\text{O}_3}$$
 (4)

$$\Delta E_{\text{Hads}} = E_{\text{H-In}_2\text{O}_3} - E_{\text{In}_2\text{O}_3} - \frac{1}{2}E_{\text{H}_2}$$
 (5)

RESULTS AND DISCUSSION

By varying the In precursor, it was possible to synthesize both c-In₂O₃ and h-In₂O₃ polymorphs. As shown in the XRD patterns in Figure 1a, c-In2O3 exhibits a main reflection at 30.6°, which is assigned to the (222) lattice plane (JCPDS, no. 06-0416). The h-In₂O₃ sample shows distinct diffraction peaks at 31.0 and 32.6°, corresponding to the (104) and (110) crystal planes (JCPDS, no. 22-0336). The morphologies of c-In₂O₃ and h-In₂O₃ were determined by SEM (Figure S1) and high-resolution TEM (Figure 1b-e). As shown in the TEM images, c-In₂O₃ nanoparticles show polyhedron characteristics with an average particle size of around 50 nm and a lattice spacing of 0.29 nm (Figure 1c) corresponding to the (222) planes, which is consistent with XRD results showing that c-In₂O₃ mainly exposes the (222) facet. For h-In₂O₃, Figures S1 and 1d show that the as-prepared h-In2O3 nanorods have a diameter of 20-50 nm and a length up to 100 nm.51 The (110) planes of h-In₂O₃ can be identified in Figure 1e. Phasepure c-In2O3 and h-In2O3 catalysts with different exposed facets provide a unique platform to compare the catalytic performance on different surfaces and thus help build the structure-activity relationship of In₂O₃ catalysts.

We next examined the catalytic performance of c-In₂O₃ and h-In₂O₃ in the RWGS reaction. As shown in Figure 2a, the RWGS rate of c-In₂O₃ is higher than that of h-In₂O₃ at 450 °C (CO selectivity > 99%). It is worthy to note that as the reaction progresses, the activity of h-In₂O₃ increases gradually, while that of c-In₂O₃ remains constant, which likely suggests a changing surface structure on h-In₂O₃ but a constant surface structure on c-In₂O₃. After 4 h on stream, the CO formation rates of both catalysts are almost the same, which likely suggests that these two catalysts have the same surface structure after 4 h. As shown in the XRD patterns in Figure 2b, the crystal phase of c-In2O3 did not change after 4 h of the RWGS reaction, consistent with the proposed constant surface structure. While for h-In₂O₃, almost all h-In₂O₃ has turned into the cubic phase, suggesting that a significant phase transition from h-In2O3 to c-In2O3 occurred during the RWGS reaction (Figure S2).

In order to confirm the crystal phase transition occurred under RWGS conditions, in situ XRD measurements were performed on h-In $_2$ O $_3$ at 450 °C. As shown in Figure 3a, phase transition was first observed on the h-In $_2$ O $_3$ surface, and as the reaction proceeds, the reflection at 30.6° corresponding to the (222) crystal plane of c-In $_2$ O $_3$ grows (Figure S3). Furthermore, the morphologies of the spent h-In $_2$ O $_3$ catalyst were determined by HRTEM. As shown in Figure 3b, the nanorod morphology remains the same after the RWGS reaction for 2 h at 450 °C. The lattice spacings of 0.397 and 0.292 nm were observed, which correspond to the (012) crystal plane of h-In $_2$ O $_3$ and the (222) crystal plane of c-In $_2$ O $_3$, respectively, consistent with the in situ XRD results confirming the phase transition from h-In $_2$ O $_3$ to c-In $_2$ O $_3$.

A series of control experiments were performed to gain insight into the phase transition. As shown in Figure 4a, no phase transition was observed with N_2 treatment at 450 $^{\circ}$ C,

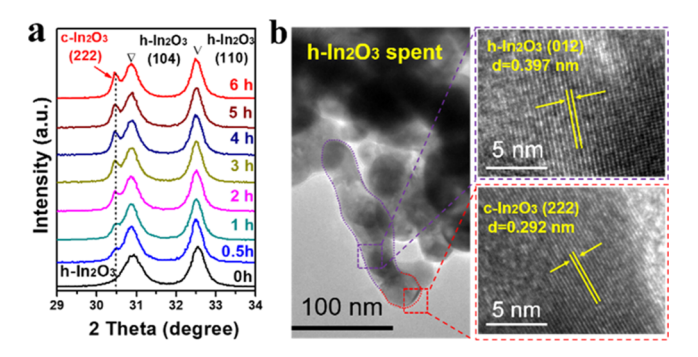


Figure 3. (a) In situ XRD patterns of h-In $_2O_3$ during the RWGS reaction and (b) HRTEM images of h-In $_2O_3$ after the RWGS reaction. Reaction conditions: 450 °C, TOS = 2 h, GHSV = 18 000 mL/g/h, H $_2$ /CO $_2$ = 2, P = 0.1 MPa.

suggesting the absence of thermally induced phase transition. Similarly, CO₂ treatment did not lead to any detectable phase transition. As shown in Figure S4, we determined the thermodynamic phase transition temperature of h-In₂O₃ with in situ XRD and found that 550 °C was the lowest temperature where thermodynamic phase transition occurs. H2 treatment in the absence of CO₂ led to full reduction of In₂O₃ to In(0) without any detectable amount of c-In2O3. These results suggest that the phase transition (from h-In₂O₃ to c-In₂O₃) occurs only during the RWGS reaction, in which both CO2 and H₂ are present. Because control experiments eliminate the possibility of thermally induced phase transition, we next focused on possible chemically induced phase transition. As suggested by the XRD results, CO2 does not react with h- In_2O_3 , but H_2 reduces h- In_2O_3 to In(0), which can be oxidized with CO₂ to c-In₂O₃ (because of the thermal stability of c- In_2O_3), as shown in the XRD results in Figure 4b. It is possible that the phase transition occurs through h-In₂O₃ \rightarrow In(0) \rightarrow c- In_2O_3 . We did not see the presence of In(0) in the in situ XRD under RWGS conditions at 450 °C, but this does not rule out the possibility of the phase transition going through In(0) because In(0) is molten (amorphous) at 450 °C and might be more rapidly oxidized by CO₂ than the reduction of h-In₂O₃ to In(0). With operando XAS-XRD and in situ TEM, Müller et al. observed that under reaction conditions, the structure of the In₂O₃ catalyst is highly dynamic, leading to a reductive amorphization and a continuous interconversion between In(0) and crystalline In₂O₃ domains, ⁶² which provides an explanation of the absence of In(0) diffraction in the in situ XRD results. To eliminate the possible oxidation of In(0) with a trace amount of O2 in the CO2 feed, gas chromatography analysis was performed simultaneously with the XRD control experiments. As shown in Figure S5, CO was observed after exposing In(0) with CO₂, which confirms that CO₂ oxidizes In(0) to c-In₂O₃. It is worthy to note that CO produced through the RWGS reaction can also reduce In₂O₃. However, as shown in Figure S6a, H2 plays a more important role in the reduction, likely because of a much higher partial pressure of H_2 (\geq 49%) than CO (\leq 7%) under reaction conditions (CO₂) conversion is about 25%). In addition to CO₂, another weak oxidant, H2O, is also present, as it is generated by the RWGS reaction. However, as shown in Figure S6b, H2O plays a less important role in oxidizing In(0) to c-In2O3, likely because of the higher partial pressure of CO_2 ($\geq 21\%$) than that of H_2O $(\leq 7\%)$. It is worthy to note that there is another possibility that In_2O_x (x < 3, another way to indicate the presence of

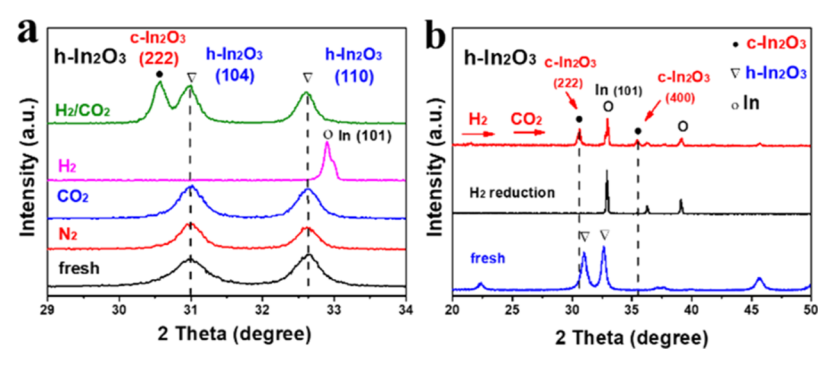


Figure 4. (a,b) XRD patterns of h-In₂O₃ after different gas treatments. Conditions: 450 °C, GHSV = 18 000 mL/g/h, P = 0.1 MPa.

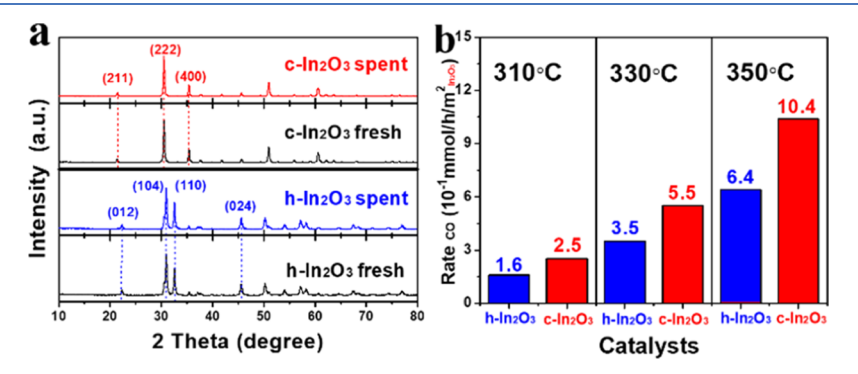


Figure 5. (a) XRD patterns of $c-In_2O_3$ and $h-In_2O_3$ (fresh and spent). (b) Rate for CO formation over $c-In_2O_3$ and $h-In_2O_3$. Reaction conditions: GHSV = 18 000 mL/g/h, H_2/CO_2 = 2, P = 0.1 MPa, CO selectivity > 99%.

oxygen vacancies) is the intermediate of phase transition at 450 °C. If x is very close to 3, we suspect that healing the oxygen vacancies with CO₂ regenerates h-In₂O₃. This is most likely to that at 300 °C based on our subsequent results. At 450 °C, x is likely much smaller than 3 [when x = 0, In₂O_x = In(0)], and healing the oxygen vacancies on In₂O_x before its further reduction to In(0) may generate c-In₂O₃. At present, we cannot rule out any one of these two possibilities. The phase transition provides a possible explanation of the increasing turn-over frequency (TOF) in RWGS at 450 °C. However, to quantitatively compare the RWGS performance of h-In₂O₃ and c-In₂O₃ and thus to build the structure—performance relationship, it is necessary to study the catalysis under conditions where no phase transition occurs.

As shown in the in situ XRD results at various temperatures in Figure S7 under the RWGS reaction conditions, the phase transition is much faster at higher temperature. At 500 °C, the phase transition is almost complete in about 5 min. While at 400 °C, no significant phase transition was observed in 3 h on stream. Therefore, we investigated the catalytic performance of c-In₂O₃ and h-In₂O₃ catalysts at low temperatures (300-350 °C), where no phase transition occurs, as confirmed with the XRD results of the spent catalysts shown in Figure 5a. It is also worthy to note that no sintering of the catalysts occurs under these conditions as confirmed by the N2 adsorption and SEM results (Table 1 and Figure S8). For both c-In₂O₃ and h-In₂O₃, the spent catalysts have the same specific surface area as the fresh ones, c- In_2O_3 (11 m²/g) and h- In_2O_3 (13 m²/g), as well as the morphologies determined by SEM (Figure S8), which provides an opportunity for an easy comparison of these two catalysts. As shown in Figure 5b, the RWGS rate over c-In₂O₃ is about 1.6 times that of h-In₂O₃ within a temperature range of 300-350 °C, similar to the observed trend at 450 °C (Figure 2a). As shown in Figure S9, the apparent activation

Table 1. Textural Properties of Selected Samples

| sample | | $S_{\rm BET}~({\rm m}^2/{\rm g})$ | total pore volume (cm²/g) |
|-------------|-------|-----------------------------------|---------------------------|
| $c-In_2O_3$ | fresh | 11 | 0.2 |
| | spent | 11 | 0.2 |
| $h-In_2O_3$ | fresh | 13 | 0.2 |
| | spent | 13 | 0.2 |

energies over $c\text{-In}_2O_3$ and $h\text{-In}_2O_3$ are different for the RWGS reaction, and the reaction orders for the CO formation rate in CO_2 and H_2 were also determined (Figure S10).

To gain insight into the catalytic performances over different crystal phases, we investigated c-In₂O₃ and h-In₂O₃ using DFT. DFT calculations suggest that CO₂ activation at oxygen vacancy sites is kinetically inhibited and is thus rate-limiting and that CO2 adsorption on oxygen vacancies is more favorable on c-In₂O₃ compared to that on h-In₂O₃. Importantly, H2 adsorbs more readily over c-In2O3, facilitating oxygen vacancy formation. Such reaction mechanisms for $\rm CO_2$ hydrogenation on $\rm In_2O_3$ have been studied previously, 38,40,44,48 where surface hydrogen coverage and oxygen vacancy formation have been identified as key players affecting reactivity toward RWGS. CO₂ adsorption can be promoted by the formation of oxygen vacancies on In₂O₃, although it has also been shown that CO₂ adsorption is more favorable on the hydroxylated c-In₂O₃(110) surface in the absence of oxygen vacancies.²² Here, we investigate a reaction mechanism involving CO2 activation in a surface oxygen vacancy, as shown in Figure 6. This mechanism begins with H₂ dissociatively adsorbing on the surface (steps a and b) and then reacting with a surface oxygen to form an oxygen vacancy and one water molecule (step c). Subsequently, CO₂ adsorbs on the oxygen vacancy (step d) and heals the vacancy by desorbing CO (step e). We also considered an alternative

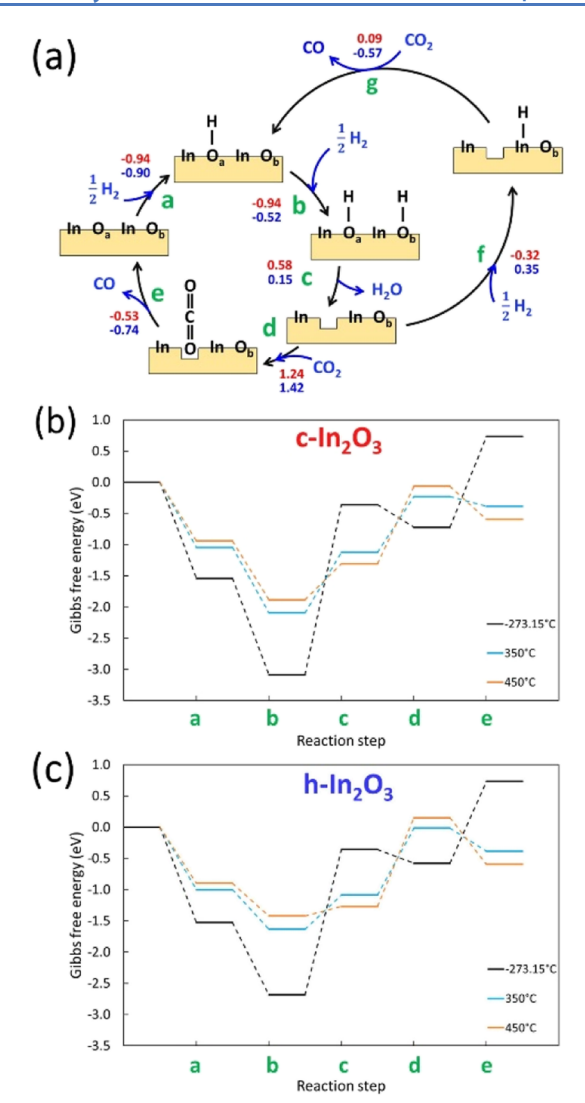


Figure 6. (a) Investigated reaction mechanism for the RWGS reaction on In_2O_3 surfaces. O_a represents the most favorable site to form an O vacancy and to adsorb hydrogen atoms, while O_b is the nearestneighbor surface O atom closest to O_a . Reaction Gibbs free energies are computed under the reaction conditions in Figure 2 with CO_2 conversion of $\sim 0.1\%$ (450 °C and partial pressures for CO_2 , H_2 , CO, and H_2O are 0.56, 1.12, 5.6 \times 10⁻⁴, and 5.6 \times 10⁻⁴ atm, respectively). Energies over c- $In_2O_3(111)$ are shown in the red text and over h- $In_2O_3(110)$ in the blue text, while the units are in electronvolt. Reaction Gibbs free energy under various reaction temperatures, for example, -273.15, 350, and 450 °C, on (b) c- $In_2O_3(111)$ and (c) h- $In_2O_3(110)$.

pathway after the oxygen vacancy formation in which additional H adsorption occurs on the In atom next to the O vacancy (step f) and CO_2 is reduced to CO with the assistance of the additional H atom (step g). The overall reaction can be divided into three parts for further discussion: H adsorption (steps a and b), O vacancy formation (step c), and CO_2 reduction (steps d and e or steps f and g).

We first computed hydrogen adsorption energies ($\Delta E_{\rm Hads}$) and oxygen vacancy formation energies ($\Delta E_{\rm Ovac}$) on all surface oxygen atom sites. We chose the c-In₂O₃(111) and h-In₂O₃(110) surfaces (Figure 7) because they are most prominent XRD features identified in Figure 1 and also because these are the most stable surfaces of each polymorph.⁵⁷ $\Delta E_{\rm Ovac}$ and $\Delta E_{\rm Hads}$ for each site are listed in

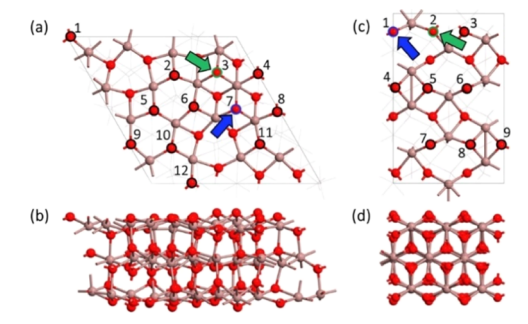


Figure 7. Top/side view of (a)/(b) c-In $_2O_3(111)$ and (c)/(d) h-In $_2O_3(110)$. The blue arrows point to the most favorable site to form an O vacancy and to adsorb a H atom. The green arrows point to the nearest-neighboring O atom to the most favorable H adsorption site. (Oxygen is shown in red and indium is shown in brown.)

Table S1, which shows that the sites that most favorably adsorb H also most favorably form an O vacancy, as expected. In Figure 7, we highlight the most favorable sites for oxygen vacancy formation in blue and the nearest-neighbor oxygen atom in green. We take these adjacent sites to be the location of dissociative H2 adsorption at the onset of the investigated RWGS reaction cycle. The most favorable sites are found to cluster together on the c-In₂O₃(111) surface (i.e., sites 3, 4, and 7 in Figure 7a) in agreement with the behavior reported by Albani et al., 50 whereas the favorable H adsorption sites are distant from each other on the h-In₂O₃(110) surface (i.e., sites 1, 6, and 7 in Figure 7c). We posit that this surface oxygen arrangement facilities H₂ adsorption on c-In₂O₃(111) compared to that on h-In₂O₃(110), as the most favorable H adsorption sites are in close proximity on c-In₂O₃(111) providing sites for rapid H₂ dissociation and oxygen vacancy formation.

We computed the reaction energy of each step (Figure 6) to understand key differences in RWGS activity at 450 °C when CO₂ conversion is 0.1%, which was chosen to represent the experimental reaction conditions. The first part of the reaction, H adsorption, exhibits a critical difference in RWGS reactivity between c-In₂O₃ and h-In₂O₃. In step a, both substrates have comparable H binding strengths (at site 7 on the cubic surface and at site 1 on the hexagonal surfaces); however, site 2 on h- $In_2O_3(110)$ binds H less favorably by 0.42 eV compared to site 3 on c- $In_2O_3(111)$. Thus, we expect that dissociative H_2 adsorption will occur more readily over the c-In₂O₃ surface. Another key difference between the polymorphs is evident in the CO₂ reduction sequence, which we consider to be ratedetermining because CO₂ adsorption (step d) is the most endergonic step under reaction temperatures (e.g., $T \ge 450$ °C). According to the reaction Gibbs free energy of step d, c-In₂O₃(111) exhibits stronger CO₂ adsorption than h-In₂O₃(110), which leads to higher reactivity because the surface can more readily activate CO₂. In the alternate CO₂ reduction pathway proceeding through steps f and g, CO₂ adsorption over h-In₂O₃(110) is more exergonic compared to that over c-In₂O₃(111). However, the preceding H adsorption step on the In atom at the oxygen vacancy (step f) is not favorable over h-In₂O₃(110), while it is favorable over the c-In₂O₃(111) surface. Furthermore, a high reaction barrier is expected in step g because of the complex geometry rearrangement required for CO₂ to concertedly abstract the adsorbed H atom and desorb CO. These results suggest that RWGS over c-In₂O₃ can be attributed primarily to an ACS Catalysis pubs.acs.org/acscatalysis Research Article

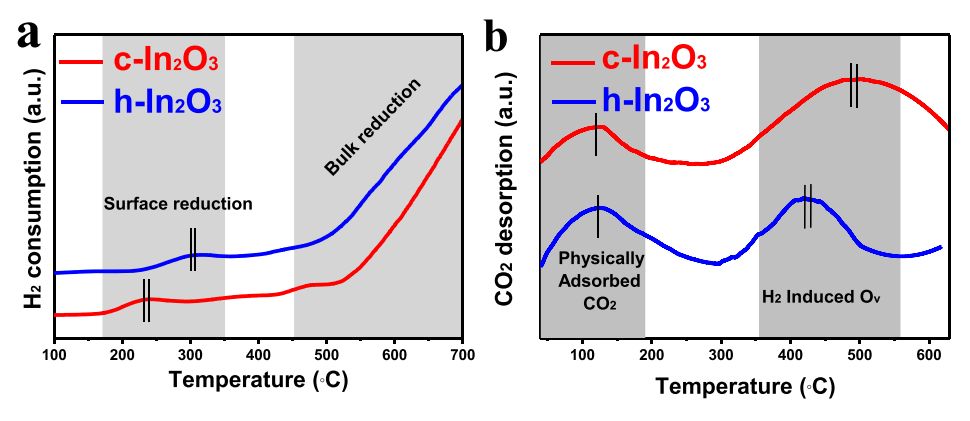


Figure 8. (a) H₂-TPR and (b) CO₂-TPD profiles of c-In₂O₃ and h-In₂O₃ catalysts.

enhanced ability to dissociatively adsorb H_2 , which in turn enhances the surface's ability to adsorb and activate CO_2 .

To investigate the temperature dependence in reactivity, we calculated the reaction Gibbs free energy at various temperatures (i.e., -273.15, 310, 330, 350, and 450 °C), which are illustrated in Figure 6b,c and listed in Tables S2 and S3 for c-In₂O₃ and h-In₂O₃, respectively. We found that the ratedetermining step changes with temperature on c-In₂O₃. At low temperature (e.g., $T \leq 350$ °C), the desorption of water (step c) becomes more endergonic than CO₂ adsorption (step d). This phenomenon is not observed on h-In₂O₃ under the reaction temperature range but is expected at lower temperature because step c dominates the reaction rate at -273.15 °C. This suggests that water release and oxygen vacancy formation can become rate-limiting at low temperatures. We also consider the reaction Gibbs free energy when partial pressures of the chemicals are all at 1 atm (Tables S4 and S5), which shows that the transition of the rate-determining step from H₂O desorption to CO₂ adsorption occurs between 330 and 350 °C on h-In2O3 and between 350 and 450 °C on c-In₂O₃ at higher conversions when the partial pressures of reactants and products are comparable.

We employed the Dudarev's DFT + U formalism with a Uvalue of 7 eV on In d states to test the sensitivity of these results with respect to known GGA deficiencies in handling localized states in oxides (Table S6). 60,61 The energies of steps a, b, and c show only slight changes. CO2 adsorption on the O vacancy, step d, becomes comparable on cubic and hexagonal surfaces, while step e becomes 0.43 and 0.53 eV more favorable on c-In₂O₃ and h-In₂O₃, respectively, compared to the DFT-PBE values without U correction. A significant change in energy is observed for step f (increasing for c-In2O3 and decreasing for h-In₂O₃) and step g (decreasing on both surfaces) because of the shift in energy of the surface with one O vacancy and one adsorbed H atom, as expected because the surface is reduced and exhibits localized electrons. Although both steps f and g are favorable on hexagonal-In₂O₃, we suggest that the high barrier in step g may block this path as discussed above.

The DFT + U calculations underscore the importance of hydrogen adsorption as the key difference between the two polymorphs, which is a trend that does not change with application of the U correction. Conversely, the CO_2 adsorption energy becomes comparable on the two polymorphs with the U correction, suggesting that this step may exhibit similar energetics over both surfaces. Hence, we hypothesize that differences in hydrogen adsorption, rather

than in CO₂ adsorption energy, are primarily responsible for the difference in RWGS performance. Note that although here we investigated CO₂ adsorption in oxygen vacancies, this conclusion would also hold for CO₂ adsorption on pristine surfaces induced by surface hydrogenation, as proposed by Posada-Borbón and Grönbeck,²² where the polymorph that more readily adsorbs hydrogen will also more readily activate CO₂ because it will exhibit higher hydrogen coverage. Investigation of alternative mechanisms that do not involve CO₂ activation at an oxygen vacancy, but rather on pristine surfaces in the presence of high hydrogen coverage, is underway.

To verify this conclusion experimentally, we studied the chemisorption properties of c-In₂O₃ and h-In₂O₃ by H₂-TPR and CO2-TPD, respectively. The H2-TPR profiles of both c-In₂O₃ and h-In₂O₃ are shown in Figure 8a. The reduction peaks above 450 °C correspond to the reduction of bulk In₂O₃, while those below 350 °C represent the reduction of the catalyst surface, that is, the formation of surface oxygen vacancies. 38,40 Compared to the reduction temperature of h-In₂O₃ around 300 °C, the reduction of c-In₂O₃ shifts to lower temperature (230 °C), suggesting that the generation of oxygen vacancy is much easier on c-In₂O₃ than on h-In₂O₃. Furthermore, by the estimated H₂ consumption areas on the TPR profiles, we expect that the concentration of the c-In₂O₃ surface oxygen vacancy is higher than that of h-In₂O₃, where c-In₂O₃ consumes more H₂ than h-In₂O₃ according to Table S7. This observation agrees with the DFT results and XPS results in Figure S11. The O 1s core-level spectra are displayed in Figure S11a where the peak at 531.4 eV is assigned to O atoms next to a defect (O defect). 40,46,48 As shown in Table S8, the concentration of the c-In₂O₃ (fresh and spent) surface oxygen vacancy is higher than that of h-In₂O₃, which means that on the c-In₂O₃ surface, there are more active sites compared to h-In₂O₃. Furthermore, the CO₂ adsorption properties of c-In₂O₃ and h-In₂O₃ surface were investigated by CO₂-TPD. CO₂-TPD profiles in Figure 8b can be divided into two regions: 100-150 and 400-550 °C, corresponding to the physically adsorbed CO₂ and chemically adsorbed CO₂ on the H₂-induced oxygen vacancy sites (O_v), respectively. 35,37 To study the role of oxygen vacancies, the effluent products were determined during CO₂-TPD by TPD-MS. As shown in Figure S12, a large amount of CO was observed when c-In2O3 with Ov was exposed to CO₂ at 300 °C, indicating that O_v can dissociate CO₂ under reaction conditions. Clearly, the desorption profile of c-In₂O₃ resembles that of h-In₂O₃ in the whole temperature range, except that the area of the CO₂ chemisorption peak is

bigger and shifted toward higher temperatures, which indicates that the CO_2 chemisorption at the oxygen vacancy sites on the c-In₂O₃ surface is much stronger than that on h-In₂O₃. We further investigated the TOF of CO formation over c-In₂O₃ and h-In₂O₃, where the number of active sites was determined by CO_2 -TPD, and found that the TOF on c-In₂O₃ is slightly higher (\sim 1.1 times) than that of h-In₂O₃ (Figure S13). These results are consistent with the DFT calculations, which indicate that c-In₂O₃ exhibits a higher RWGS rate than h-In₂O₃ because of its (1) facile formation of more oxygen vacancies (active sites) and (2) enhanced ability to adsorb and activate CO_2 on the oxygen vacancies.

CONCLUSIONS

In₂O₃ with different crystal phases was prepared and evaluated for the RWGS reaction. Under the high-temperature conditions (450 °C), c-In₂O₃ shows stable catalytic performance, while h-In2O3 shows an increasing catalytic activity because of the phase transition from h-In₂O₃ to c-In₂O₃. In situ XRD results suggest that the crystal phase transition occurs through two steps, first H₂ reduces h-In₂O₃ to In(0) or In₂O_x and then CO₂ oxidizes In (0) or In₂O_x to c-In₂O₃. During the low-temperature reaction (300-350 °C), both h-In₂O₃ and c-In₂O₃ are highly selective toward CO (>99%) over CH₄, while c-In₂O₃ exhibits about 1.6 times higher rate (per surface area) than that of h-In₂O₃. DFT simulations demonstrate that the higher RWGS rate over c-In2O3 can be attributed to (1) an enhanced ability to dissociatively adsorb H2, resulting from favorable surface O arrangement, and (2) an enhanced ability to adsorb and activate CO₂. Further surface analyses verify that it is easier to adsorb H2 and to form oxygen vacancies on the surface of c-In₂O₃ and that these oxygen vacancies adsorb CO₂ stronger than on the h-In₂O₃ surface. Our results demonstrate the importance of crystal structures for catalytic performance. These results may be extended to other catalytic systems to design catalysts for important chemical reactions.

ASSOCIATED CONTENT

Supporting Information

The Supporting Information is available free of charge at https://pubs.acs.org/doi/10.1021/acscatal.9b04239.

SEM images, XRD results, XPS results, and additional kinetic and DFT data (PDF)

AUTHOR INFORMATION

Corresponding Authors

Guanghui Zhang — State Key Laboratory of Fine Chemicals, PSU-DUT Joint Center for Energy Research, School of Chemical Engineering, Dalian University of Technology, Dalian 116024, P. R. China; ◎ orcid.org/0000-0002-5854-6909; Email: gzhang@dlut.edu.cn

Xinwen Guo — State Key Laboratory of Fine Chemicals, PSU-DUT Joint Center for Energy Research, School of Chemical Engineering, Dalian University of Technology, Dalian 116024, P. R. China; ⊚ orcid.org/0000-0002-6597-4979; Email: guoxw@dlut.edu.cn

Chunshan Song — State Key Laboratory of Fine Chemicals, PSU-DUT Joint Center for Energy Research, School of Chemical Engineering, Dalian University of Technology, Dalian 116024, P. R. China; EMS Energy Institute, Department of Energy & Mineral Engineering and Chemical Engineering, PSU-DUT Joint Center for Energy Research, Pennsylvania State University,

University Park, Pennsylvania 16802, United States; orcid.org/0000-0003-2344-9911; Email: csong@psu.edu

Authors

Jianyang Wang — State Key Laboratory of Fine Chemicals, PSU-DUT Joint Center for Energy Research, School of Chemical Engineering, Dalian University of Technology, Dalian 116024, P. R. China

Chun-Yen Liu — Department of Chemical and Biomolecular Engineering, Rice University, Houston, Texas 77005, United States

Thomas P. Senftle — Department of Chemical and Biomolecular Engineering, Rice University, Houston, Texas 77005, United States; orcid.org/0000-0002-5889-5009

Jie Zhu — State Key Laboratory of Fine Chemicals, PSU-DUT Joint Center for Energy Research, School of Chemical Engineering, Dalian University of Technology, Dalian 116024, P. R. China

Complete contact information is available at: https://pubs.acs.org/10.1021/acscatal.9b04239

Author Contributions

J.W. and C.-Y.L. contributed equally to the work. The manuscript was written through contributions of all authors. All authors have given approval to the final version of the manuscript.

Notes

The authors declare no competing financial interest.

ACKNOWLEDGMENTS

This work was financially supported by the National Key Research and Development Program of China (2016YFB0600902-4), National Natural Science Foundation of China (21902019), Fundamental Research Funds for Central Universities (DUT18RC(3)057), and the Pennsylvania State University. C.-Y.L. and T.P.S. acknowledge startup funding from Rice University.

REFERENCES

- (1) Auffhammer, M.; Carson, R. T. Forecasting the path of China's CO₂ emissions using province-level information. *J. Environ. Econ. Manag.* **2008**, 55, 229–247.
- (2) Tahir, M.; Amin, N. S. Advances in visible light responsive titanium oxide-based photocatalysts for CO₂ conversion to hydrocarbon fuels. *Energy Convers. Manage.* **2013**, *76*, 194–214.
- (3) Dorner, R. W.; Hardy, D. R.; Williams, F. W.; Willauer, H. D. Heterogeneous catalytic CO₂ conversion to value-added hydrocarbons. *Energy Environ. Sci.* **2010**, *3*, 884–890.
- (4) Guo, L.; Sun, J.; Ge, Q.; Tsubaki, N. Recent advances in direct catalytic hydrogenation of carbon dioxide to valuable C₂⁺ hydrocarbons. *J. Mater. Chem. A* **2018**, *6*, 23244–23262.
- (5) Tackett, B. M.; Gomez, E.; Chen, J. G. Net reduction of $\rm CO_2$ via its thermocatalytic and electrocatalytic transformation reactions in standard and hybrid processes. *Nat. Catal.* **2019**, *2*, 381–386.
- (6) Centi, G.; Quadrelli, E. A.; Perathoner, S. Catalysis for CO₂ conversion: a key technology for rapid introduction of renewable energy in the value chain of chemical industries. *Energy Environ. Sci.* **2013**, *6*, 1711–1731.
- (7) Daza, Y. A.; Kuhn, J. N. CO₂ conversion by reverse water gas shift catalysis: comparison of catalysts, mechanisms and their consequences for CO₂ conversion to liquid fuels. *RSC Adv.* **2016**, *6*, 49675–49691.
- (8) Porosoff, M. D.; Yan, B.; Chen, J. G. Catalytic reduction of CO₂ by H₂ for synthesis of CO, methanol and hydrocarbons: challenges and opportunities. *Energy Environ. Sci.* **2016**, *9*, 62–73.

- (9) Barreiro, M. M.; Maroño, M.; Sánchez, J. M. Hydrogen permeation through a Pd-based membrane and RWGS conversion in H_2/CO_2 , $H_2/N_2/CO_2$ and $H_2/H_2O/CO_2$ mixtures. *Int. J. Hydrogen Energy* **2014**, *39*, 4710–4716.
- (10) Chen, X.; Su, X.; Duan, H.; Liang, B.; Huang, Y.; Zhang, T. Catalytic performance of the Pt/TiO₂ catalysts in reverse water gas shift reaction: Controlled product selectivity and a mechanism study. *Catal. Today* **2017**, *281*, 312–318.
- (11) Goguet, A.; Meunier, F.; Breen, J.; Burch, R.; Petch, M.; Faurghenciu, A. Study of the origin of the deactivation of a Pt/CeO₂ catalyst during reverse water gas shift (RWGS) reaction. *J. Catal.* **2004**, 226, 382–392.
- (12) Kim, S. S.; Lee, H. H.; Hong, S. C. A study on the effect of support's reducibility on the reverse water-gas shift reaction over Pt catalysts. *Appl. Catal.*, A **2012**, 423–424, 100–107.
- (13) Liang, B.; Duan, H.; Su, X.; Chen, X.; Huang, Y.; Chen, X.; Delgado, J. J.; Zhang, T. Promoting role of potassium in the reverse water gas shift reaction on Pt/mullite catalyst. *Catal. Today* **2017**, *281*, 319–326.
- (14) Liu, Y.; Li, Z.; Xu, H.; Han, Y. Reverse water-gas shift reaction over ceria nanocube synthesized by hydrothermal method. *Catal. Commun.* **2016**, *76*, 1–6.
- (15) Ro, I.; Sener, C.; Stadelman, T. M.; Ball, M. R.; Venegas, J. M.; Burt, S. P.; Hermans, I.; Dumesic, J. A.; Huber, G. W. Measurement of intrinsic catalytic activity of Pt monometallic and Pt-MoO_x interfacial sites over visible light enhanced PtMoO_x /SiO₂ catalyst in reverse water gas shift reaction. *J. Catal.* **2016**, 344, 784–794.
- (16) Sun, F.-m.; Yan, C.-f.; Wang, Z.-d.; Guo, C.-q.; Huang, S.-l. Ni/Ce–Zr–O catalyst for high CO₂ conversion during reverse water gas shift reaction (RWGS). *Int. J. Hydrogen Energy* **2015**, *40*, 15985–15993.
- (17) Wang, L.; Liu, H.; Chen, Y.; Yang, S. Reverse water—gas shift reaction over co-precipitated Co–CeO₂ catalysts: Effect of Co content on selectivity and carbon formation. *Int. J. Hydrogen Energy* **2017**, *42*, 3682–3689.
- (18) Yang, L.; Pastor-Pérez, L.; Gu, S.; Sepúlveda-Escribano, A.; Reina, T. R. Highly efficient Ni/CeO₂-Al₂O₃ catalysts for CO₂ upgrading via reverse water-gas shift: Effect of selected transition metal promoters. *Appl. Catal., B* **2018**, 232, 464–471.
- (19) Zhang, X.; Zhu, X.; Lin, L.; Yao, S.; Zhang, M.; Liu, X.; Wang, X.; Li, Y.-W.; Shi, C.; Ma, D. Highly Dispersed Copper over β -Mo₂C as an Efficient and Stable Catalyst for the Reverse Water Gas Shift (RWGS) Reaction. *ACS Catal.* **2017**, *7*, 912–918.
- (20) Zonetti, P. C.; Letichevsky, S.; Gaspar, A. B.; Sousa-Aguiar, E. F.; Appel, L. G. The $NixCe_{0.75}Zr_{0.25-x}O_2$ solid solution and the RWGS. *Appl. Catal., A* **2014**, *475*, 48–54.
- (21) Bielz, T.; Lorenz, H.; Amann, P.; Klötzer, B.; Penner, S. Water–Gas Shift and Formaldehyde Reforming Activity Determined by Defect Chemistry of Polycrystalline In₂O₃. *J. Phys. Chem. C* **2011**, 115, 6622–6628.
- (22) Posada-Borbón, A.; Grönbeck, H. CO₂ adsorption on hydroxylated In₂O₃(110). Phys. Chem. Chem. Phys. **2019**, 21, 21698–21708.
- (23) Sun, Q.; Ye, J.; Liu, C.-j.; Ge, Q. In₂O₃ as a promising catalyst for CO₂ utilization: A case study with reverse water gas shift over In₂O₃. *Greenhouse Gases: Sci. Technol.* **2014**, *4*, 140–144.
- (24) Wang, W.; Zhang, Y.; Wang, Z.; Yan, J.-m.; Ge, Q.; Liu, C.-j. Reverse water gas shift over In_2O_3 – CeO_2 catalysts. *Catal. Today* **2016**, 259, 402–408.
- (25) Rodriguez, J. A.; Liu, P.; Stacchiola, D. J.; Senanayake, S. D.; White, M. G.; Chen, J. G. Hydrogenation of CO₂ to Methanol: Importance of Metal—Oxide and Metal—Carbide Interfaces in the Activation of CO₂. ACS Catal. **2015**, *5*, 6696—6706.
- (26) Dietz, L.; Piccinin, S.; Maestri, M. Mechanistic Insights into CO₂ Activation via Reverse Water–Gas Shift on Metal Surfaces. *J. Phys. Chem. C* **2015**, *119*, 4959–4966.
- (27) Aitbekova, A.; Wu, L.; Wrasman, C. J.; Boubnov, A.; Hoffman, A. S.; Goodman, E. D.; Bare, S. R.; Cargnello, M. Low-Temperature Restructuring of CeO₂-Supported Ru Nanoparticles Determines

- Selectivity in CO₂ Catalytic Reduction. J. Am. Chem. Soc. 2018, 140, 13736–13745.
- (28) Kattel, S.; Liu, P.; Chen, J. G. Tuning Selectivity of CO₂ Hydrogenation Reactions at the Metal/Oxide Interface. *J. Am. Chem. Soc.* **2017**, *139*, 9739–9754.
- (29) Li, W.; Zhang, G.; Jiang, X.; Liu, Y.; Zhu, J.; Ding, F.; Liu, Z.; Guo, X.; Song, C. CO₂ Hydrogenation on Unpromoted and M-Promoted Co/TiO₂ Catalysts (M = Zr, K, Cs): Effects of Crystal Phase of Supports and Metal—Support Interaction on Tuning Product Distribution. ACS Catal. 2019, 9, 2739–2751.
- (30) Matsubu, J. C.; Yang, V. N.; Christopher, P. Isolated metal active site concentration and stability control catalytic CO₂ reduction selectivity. *J. Am. Chem. Soc.* **2015**, *137*, 3076–3084.
- (31) Samson, K.; Śliwa, M.; Socha, R. P.; Góra-Marek, K.; Mucha, D.; Rutkowska-Zbik, D.; Paul, J.-F.; Ruggiero-Mikołajczyk, M.; Grabowski, R.; Słoczyński, J. Influence of ZrO₂ Structure and Copper Electronic State on Activity of Cu/ZrO₂ Catalysts in Methanol Synthesis from CO₂. ACS Catal. **2014**, *4*, 3730–3741.
- (32) Kim, A.; Sanchez, C.; Patriarche, G.; Ersen, O.; Moldovan, S.; Wisnet, A.; Sassoye, C.; Debecker, D. P. Selective CO₂ methanation on Ru/TiO₂ catalysts: unravelling the decisive role of the TiO₂ support crystal structure. *Catal. Sci. Technol.* **2016**, *6*, 8117–8128.
- (33) Liu, J.-X.; Su, H.-Y.; Sun, D.-P.; Zhang, B.-Y.; Li, W.-X. Crystallographic dependence of CO activation on cobalt catalysts: HCP versus FCC. *J. Am. Chem. Soc.* **2013**, *135*, 16284–16287.
- (34) Lyu, S.; Wang, L.; Zhang, J.; Liu, C.; Sun, J.; Peng, B.; Wang, Y.; Rappé, K. G.; Zhang, Y.; Li, J.; Nie, L. Role of Active Phase in Fischer-Tropsch Synthesis: Experimental Evidence of CO Activation over Single-Phase Cobalt Catalysts. ACS Catal. 2018, 8, 7787–7798.
- (35) Dou, M.; Zhang, M.; Chen, Y.; Yu, Y. Theoretical insights into the surface structure of In_2O_3 (110) surface and its effect on methanol synthesis from CO_2 hydrogenation. *Comput. Theor. Chem.* **2018**, 1126, 7–12.
- (36) Frei, M. S.; Capdevila-Cortada, M.; García-Muelas, R.; Mondelli, C.; López, N.; Stewart, J. A.; Curulla Ferré, D.; Pérez-Ramírez, J. Mechanism and microkinetics of methanol synthesis via CO₂ hydrogenation on indium oxide. *J. Catal.* **2018**, *361*, 313–321.
- (37) García-Trenco, A.; Regoutz, A.; White, E. R.; Payne, D. J.; Shaffer, M. S. P.; Williams, C. K. PdIn intermetallic nanoparticles for the Hydrogenation of CO_2 to Methanol. *Appl. Catal., B* **2018**, 220, 9–18.
- (38) Martin, O.; Martín, A. J.; Mondelli, C.; Mitchell, S.; Segawa, T. F.; Hauert, R.; Drouilly, C.; Curulla-Ferré, D.; Pérez-Ramírez, J. Indium Oxide as a Superior Catalyst for Methanol Synthesis by CO₂ Hydrogenation. *Angew. Chem., Int. Ed.* **2016**, *55*, 6261–6265.
- (39) Richard, A. R.; Fan, M. Low-Pressure Hydrogenation of CO₂ to CH₃OH Using Ni-In-Al/SiO₂ Catalyst Synthesized via a Phyllosilicate Precursor. *ACS Catal.* **2017**, *7*, 5679–5692.
- (40) Rui, N.; Wang, Z.; Sun, K.; Ye, J.; Ge, Q.; Liu, C.-j. CO₂ hydrogenation to methanol over Pd/In₂O₃: effects of Pd and oxygen vacancy. *Appl. Catal., B* **2017**, 218, 488–497.
- (41) Snider, J. L.; Streibel, V.; Hubert, M. A.; Choksi, T. S.; Valle, E.; Upham, D. C.; Schumann, J.; Duyar, M. S.; Gallo, A.; Abild-Pedersen, F.; Jaramillo, T. F. Revealing the Synergy between Oxide and Alloy Phases on the Performance of Bimetallic In–Pd Catalysts for CO₂ Hydrogenation to Methanol. *ACS Catal.* **2019**, *9*, 3399–3412.
- (42) Sun, K.; Fan, Z.; Ye, J.; Yan, J.; Ge, Q.; Li, Y.; He, W.; Yang, W.; Liu, C.-j. Hydrogenation of CO_2 to methanol over In_2O_3 catalyst. *J.* CO_2 *Util.* **2015**, 12, 1–6.
- (43) Ye, J.; Liu, C.; Ge, Q. DFT Study of CO₂ Adsorption and Hydrogenation on the In₂O₃ Surface. *J. Phys. Chem. C* **2012**, *116*, 7817–7825.
- (44) Ye, J.; Liu, C.; Mei, D.; Ge, Q. Active Oxygen Vacancy Site for Methanol Synthesis from CO₂ Hydrogenation on In₂O₃(110): A DFT Study. ACS Catal. **2013**, 3, 1296–1306.
- (45) Ye, J.; Liu, C.-j.; Mei, D.; Ge, Q. Methanol synthesis from CO_2 hydrogenation over a Pd4/In₂O₃ model catalyst: A combined DFT and kinetic study. *J. Catal.* **2014**, *317*, 44–53.

- (46) Dang, S.; Gao, P.; Liu, Z.; Chen, X.; Yang, C.; Wang, H.; Zhong, L.; Li, S.; Sun, Y. Role of zirconium in direct CO_2 hydrogenation to lower olefins on oxide/zeolite bifunctional catalysts. *J. Catal.* **2018**, 364, 382–393.
- (47) Gao, J.; Jia, C.; Liu, B. Direct and selective hydrogenation of CO₂ to ethylene and propene by bifunctional catalysts. *Catal. Sci. Technol.* **2017**, *7*, 5602–5607.
- (48) Gao, P.; Li, S.; Bu, X.; Dang, S.; Liu, Z.; Wang, H.; Zhong, L.; Qiu, M.; Yang, C.; Cai, J.; Wei, W.; Sun, Y. Direct conversion of CO_2 into liquid fuels with high selectivity over a bifunctional catalyst. *Nat. Chem.* **2017**, *9*, 1019–1024.
- (49) Su, J.; Wang, D.; Wang, Y.; Zhou, H.; Liu, C.; Liu, S.; Wang, C.; Yang, W.; Xie, Z.; He, M. Direct Conversion of Syngas into Light Olefins over Zirconium-Doped Indium(III) Oxide and SAPO-34 Bifunctional Catalysts: Design of Oxide Component and Construction of Reaction Network. *ChemCatChem* **2018**, *10*, 1536–1541.
- (50) Albani, D.; Capdevila-Cortada, M.; Vilé, G.; Mitchell, S.; Martin, O.; López, N.; Pérez-Ramírez, J. Semihydrogenation of Acetylene on Indium Oxide: Proposed Single-Ensemble Catalysis. *Angew. Chem., Int. Ed.* **2017**, *56*, 10755–10760.
- (51) Xu, J.; Chen, Y.; Shen, J. Ethanol sensor based on hexagonal indium oxide nanorods prepared by solvothermal methods. *Mater. Lett.* **2008**, *62*, 1363–1365.
- (52) Kresse, G.; Furthmüller, J. Efficient iterative schemes forab initiototal-energy calculations using a plane-wave basis set. *Phys. Rev. B: Condens. Matter Mater. Phys.* **1996**, *54*, 11169–11186.
- (53) Blöchl, P. E. Projector augmented-wave method. *Phys. Rev. B: Condens. Matter Mater. Phys.* **1994**, *50*, 17953–17979.
- (54) Kresse, G.; Joubert, D. From ultrasoft pseudopotentials to the projector augmented-wave method. *Phys. Rev. B: Condens. Matter Mater. Phys.* **1999**, 59, 1758–1775.
- (55) Perdew, J. P.; Burke, K.; Ernzerhof, M. Generalized Gradient Approximation Made Simple. *Phys. Rev. Lett.* **1996**, *77*, 3865–3868.
- (56) Monkhorst, H. J.; Pack, J. D. Special points for Brillouin-zone integrations. *Phys. Rev. B: Condens. Matter Mater. Phys.* **1976**, 13, 5188–5192.
- (57) Walsh, A.; Catlow, C. R. A. Structure, stability and work functions of the low index surfaces of pure indium oxide and Sndoped indium oxide (ITO) from density functional theory. *J. Mater. Chem.* **2010**, 20, 10438–10444.
- (58) Grimme, S.; Antony, J.; Ehrlich, S.; Krieg, H. A consistent and accurate ab initio parametrization of density functional dispersion correction (DFT-D) for the 94 elements H-Pu. *J. Chem. Phys.* **2010**, 132, 154104.
- (59) Hinnemann, B.; Carter, E. A. Adsorption of Al, O, Hf, Y, Pt, and S Atoms on r-Al₂O₃(0001). *J. Phys. Chem. C* **2007**, *111*, 7105–7126.
- (60) Dudarev, S. L.; Botton, G. A.; Savrasov, S. Y.; Humphreys, C. J.; Sutton, A. P. Electron-energy-loss spectra and the structural stability of nickel oxide: An LSDA+U study. *Phys. Rev. B: Condens. Matter Mater. Phys.* 1998, 57, 1505–1509.
- (61) Erhart, P.; Klein, A.; Egdell, R. G.; Albe, K. Band structure of indium oxide: Indirect versus direct band gap. *Phys. Rev. B: Condens. Matter Mater. Phys.* **2007**, 75, 153205.
- (62) Tsoukalou, A.; Abdala, P. M.; Stoian, D.; Huang, X.; Willinger, M.-G.; Fedorov, A.; Müller, C. R. Structural Evolution and Dynamics of an In₂O₃ Catalyst for CO₂ Hydrogenation to Methanol: An Operando XAS-XRD and In Situ TEM Study. *J. Am. Chem. Soc.* **2019**, *141*, 13497–13505.